crystals

MDPI

Article

Large-Scale Production and Optical Properties of a High-Quality SnS_2 Single Crystal Grown Using the Chemical Vapor Transportation Method

Prashant Tripathi [1,2,*], Arun Kumar [3,†], Prashant K. Bankar [4], Kedar Singh [2] and Bipin Kumar Gupta [1,*]

[1] Photonic Materials Metrology Sub Division, Advanced Materials and Device Metrology Division, CSIR-National Physical Laboratory, Dr. K. S. Krishnan Marg, New Delhi 110012, India
[2] School of Physical Sciences, Jawaharlal Nehru University, New Delhi 110067, India; kedarbhu08@gmail.com
[3] CNR—Institute for Microelectronics and Microsystems, Via C. Olivetti 2, 20864 Agrate Brianza, Italy; akumar@unisa.it
[4] Centre for Advanced Studies in Materials Science and Condensed Matter Physics, Department of Physics, Savitribai Phule Pune University, Pune 411007, India; bankarprashant26@gmail.com
* Correspondence: pra.jest01@gmail.com (P.T.); bipinbhu@yahoo.com (B.K.G.)
† Current address: Department of Physics "E.R. Caianiello", University of Salerno, Via G. Paollo I 132, 84084 Salerno, Italy.

Abstract: The scientific community believes that high-quality, bulk layered, semiconducting single crystals are crucial for producing two-dimensional (2D) nanosheets. This has a significant impact on current cutting-edge science in the development of next-generation electrical and optoelectronic devices. To meet this ever-increasing demand, efforts have been made to manufacture high-quality SnS_2 single crystals utilizing low-cost CVT (chemical vapor transportation) technology, which allows for large-scale crystal production. Based on the chemical reaction that occurs throughout the CVT process, a viable mechanism for SnS_2 growth is postulated in this paper. Optical, XRD with Le Bail fitting, TEM, and SEM are used to validate the quality, phase, gross structural/microstructural analyses, and morphology of SnS_2 single crystals. Furthermore, Raman, TXRF, XPS, UV–Vis, and PL spectroscopy are used to corroborate the quality of the SnS_2 single crystals, as well as the proposed energy level diagram for indirect transition in the bulk SnS_2 single crystals. As a result, the suggested method provides a cost-effective method for growing high-quality SnS_2 single crystals, which could lead to a new alternative resource for producing 2D SnS_2 nanosheets, which are in great demand for designing next-generation optoelectronic and quantum devices.

Keywords: tin disulfides; chemical vapor transport; high-quality; large scale; single crystal

Citation: Tripathi, P.; Kumar, A.; Bankar, P.K.; Singh, K.; Gupta, B.K. Large-Scale Production and Optical Properties of a High-Quality SnS_2 Single Crystal Grown Using the Chemical Vapor Transportation Method. *Crystals* **2023**, *13*, 1131. https://doi.org/10.3390/cryst13071131

Academic Editor: Wolfram Miller

Received: 6 July 2023
Revised: 16 July 2023
Accepted: 18 July 2023
Published: 20 July 2023

1. Introduction

Layered metal dichalcogenide semiconductors [1–14] have recently gained intensive interest worldwide due to their remarkable electrical, thermal, mechanical, and optical properties [15–18]. As a result, they have shown potential applications in various fields including field-effect transistors (FETs) [19,20], photodetectors [21], solar cells [22], sensors, and flexible devices [23]. Among them, tin disulfide (SnS_2) is a layered semiconductor with a distinctive crystal structure in which tin atoms are sandwiched between two layers of hexagonally packed sulfur atoms, with strong covalent connections connecting in-plane Sn-S bonds and van der Waals forces weakly coupling S-Sn-S layers. Due to its wide bandgap (~2.2 eV), layered structure, high absorption coefficient (10^5–10^6 cm^{-1}), large carrier mobility (230 cm^2 V^{-1} s^{-1}) [24–26], earth abundance, and environmentally friendly nature, tin disulfide (SnS_2) is very popular in electronic [27–29], optoelectronic [30–33], and energy storage and conversion applications [34–36]. It is a good contender for FETs, integrated logic circuits, and photodetectors [25,37,38] due to its wide bandgap, which may

allow it to benefit from suppressing drain to source tunneling for short channels. SnS_2-based photodetectors, in particular, demonstrate outstanding responsivity, a large on/off ratio, quick response, and strong stability, making them highly promising for optoelectronic applications [25]. Monolayer SnS_2, with its high mobility [39] and quick photocurrent response [40–42], has recently been shown to be competitive and promising for electrical and optical devices. SnS_2 also has an adjustable bandgap in the visible region, similar to MoS_2, with thicknesses spanning from bulk to monolayer ranging from 2.0 to 2.4 eV, but it is an indirect bandgap semiconductor at all thicknesses. SnS_2, like MoS_2, has broadband absorption properties with absorption characteristics at 1550 nm [43,44], necessitating a thorough investigation of their optical performance, which is still in its infancy. The broad bandgap range of SnS_2 has enormous potential in electrical applications [45].

Material properties vary extensively with the preparation method and, consequently, morphology and microstructures. Single crystals of tin disulfide have been grown using the Bridgman method and chemical vapor transport [46,47]; thin films can be created using chemical vapor deposition [47], chemical bath deposition [48], atomic layer deposition [49], electrodeposition [50], the sulfurization of tin films [51], solid-state multilayer synthesis [52], and successive ionic layer adsorption and reaction [53]. The chemical vapor transport (CVT) method offers several advantages over the Bridgman method for the growth of single crystals of tin disulfide (SnS_2). The CVT method for growing SnS_2 single crystals offers advantages in terms of lower growth temperatures, enhanced control of vapor composition, scalability, reproducibility, versatility in growth techniques, and reduced contamination. The CVT method allows for crystal growth at lower temperatures compared to the Bridgman method because it utilizes volatile species that can be transported at lower temperatures in the form of gas or vapor. In addition, lower growth temperatures can reduce thermal stresses and minimize the occurrence of crystal defects, leading to higher crystal quality. Moreover, in CVT, the transporting agent can be precisely controlled to optimize the vapor composition during crystal growth. By adjusting the composition of the transporting gas or vapor, it is possible to influence the growth kinetics, crystal structure, and impurity incorporation. This level of control can result in better crystal quality and desired properties of the SnS_2 single crystals. Compared to the Bridgman method, the CVT method often involves a closed system or sealed ampoule, which helps in minimizing contamination from external sources during crystal growth. This controlled environment reduces the likelihood of impurities being incorporated into the crystal lattice, resulting in higher-purity single crystals. These advantages make CVT a widely used and effective approach for producing high-quality SnS_2 crystals for various scientific and technological applications. Chemical vapor transport is one of the most widely used methods for producing massive and high-quality SnS_2 single crystals. The CVT method allows for the growth of high-quality single crystals by providing a controlled vapor transport process. The use of a transporting agent facilitates the formation of volatile compounds, lowering the required temperatures for vaporization and crystal growth. The precise control of temperature, pressure, and composition during the CVT process enables the production of massive, high-quality SnS_2 single crystals suitable for various applications. Schäfer was the one who first put forth CVT as a means of vaporizing metals at lower temperatures by producing a volatile chemical intermediate [54]. Iodine has been demonstrated to be the best carrier agent for tin [55], and it has been effectively used with copper zinc tin sulfide (CZTS) single crystals [56].

Growing single crystals in the laboratory and subsequently preparing thin films or crystals from them using various methods, such as mechanical exfoliation, the solution-processed method, and so on, is a preferred approach due to its cost-effectiveness, control over crystal quality, tunable thickness and lateral size, scalability, and versatility. These advantages make it an attractive method for obtaining high-quality nanocrystals/sheets, such as SnS_2, on a large scale while allowing for customization to meet specific application requirements. The primary goal of this study, as stated in this article, is to use the CVT approach to grow high-quality and large-scale SnS_2 single crystals.

2. Materials and Methods

2.1. Experimental Details

The iodine vapor transport technique was employed for the growth of the single crystals of SnS_2. For growing a single crystal of SnS_2, the stoichiometric proportion of the pure elements Sn and S was placed inside a sealed quartz tube. A quartz tube with an inner diameter of 1.5 cm and a length of 20 cm, and a bore constriction of 2 to 3 mm at the end of sealing was used. A little amount of iodine (0.2 g) was kept inside the tube as a transporter [55]. An amount of 1.30 g of Sn (99.99% purity; Sigma-Aldrich, St. Louis, MO, USA) and 0.70 g of S (99.998% purity; Sigma-Aldrich) were taken for the growth of SnS_2. The quartz tube was evacuated to a pressure of 10^{-5} torr using an oil diffusion pump and then sealed by placing the lower portion of the tube in a liquid nitrogen bath to avoid any material volatilization or sublimation during the sealing process. The charged sealed ampoule was then placed in a two-zone furnace with the charged and sealed ends facing hotter and cooler zones, respectively. The furnace presents a temperature gradient along the axis and several hours (41 h) of reactions resulted in the growth of a single crystal of SnS_2 at the colder empty end of the ampoule. The reaction zone (T_1) was held at 963 K, the growth zone (T_2) was kept at 823 K, and the furnace was run for 41 h. Large crystals of typically flaky forms grew and gathered near the colder end of the ampoule during this time. The furnace was turned off and allowed to cool to a normal temperature once the reaction was completed. The ampoule was cut down and the crystals were removed for further processing.

2.2. Characterizations

The X-ray diffraction (XRD) pattern was recorded using a PANalytical Empyrean instrument, which is equipped with a 2D detector and a graphite monochromator and has a Cu-Kα_1 beam (wavelength ~1.54056 Å). The XRD patterns of the as-grown SnS_2 flakes were studied to establish their gross structure. The VESTA software was employed to generate the crystal structure. A Renishaw inVia spectrometer with the excitation wavelengths of 355 and 514 nm lines of a continuous UV and green laser, respectively, was used to perform micro-Raman spectroscopy in a z-backscattering geometry. A 50× objective (long working distance) with a numerical aperture close to 0.75 was utilized to focus the laser on the sample surface. All of the tests were completed at room temperature (RT). The FEI Tecnai G^2 was used to capture transmission electron micrographs and SAED data (accelerating voltage: 200 kV). A modest amount of SnS_2 crystals were sonicated in ethanol for 1 h before being drop-casted onto a carbon grid for sample preparation. Finally, under the light of a table lamp, the sample was dried. An X-ray total reflection spectrometer fitted with a Mo-K_α radiation source was used to perform total reflection X-ray fluorescence (TXRF) measurements. The ratio of tin and sulfur, L, and K lines, respectively, was used to determine the elemental composition of the SnS_2 crystals. X-ray photoelectron spectroscopy (XPS) measurements were carried out on an Al Kα X-ray PHI VersaProbe III instrument. The C 1s peak at 284.5 eV, which was caused by adventitious carbon, served as the reference point for all binding energies in the XPS spectra. The photoluminescence (PL) spectrum was obtained using the micro-Raman spectrometer with an excitation wavelength of 355 nm, as the inVia confocal Raman microscope is capable of acquiring both Raman scattering and PL. The photoluminescence spectra of the SnS_2 crystals were investigated using a Horiba Yvon FluroMax-4 Spectrofluorometer equipped with a solid-state laser with a maximum exciting laser power of 4 mW. The PL spectra of the SnS_2 crystals were recorded using 10% of the maximum laser power.

3. Results and Discussion

The CVT process is schematically represented in Figure 1a, with the red zone of the furnace showing a higher temperature and the yellow zone showing a lower temperature. The precursor chemicals were stored in a sealed ampule at the hotter zone in a stoichiometric proportion with iodine, as indicated by the grey color. As illustrated in Figure 1, the furnace

provided a temperature differential along the tubular axis, resulting in the growth of yellow flaky crystals in the colder zone after many hours of chemical reaction (Figure 1a). With the help of iodine, tin from the precursor migrated to the cooler ends and created tin iodide, as shown in Equation (1). Further, di-iodide (SnI_2) dissociated into tetraiodide (SnI_4) and SnS_2 formed at the growth temperature (T_2), as illustrated in Equation (2). Figure 1b shows an optical image of the sealed ampule holding a large number of SnS_2 single crystals with lateral sizes ranging from 1 to 2 cm. Nearly all of the solid precursors were transformed into crystals, and very high yields of SnS_2 were crystals are obtained, as shown in Figure 1b. The beauty of this process is that a tiny quantity of iodine transporter is enough to transport very large amounts of the solid, because SnI_4 cycles to the reaction end of the system and reacts with additional dichalcogenide; this process continues until all the charge is delivered to the growth zone.

$$2SnS_2 + 2I_2 \rightleftharpoons 2SnI_2 + 2S_2 \quad (1)$$

$$2SnI_2 + 2S_2 \rightleftharpoons SnI_4 + SnS_2 + S_2 \quad (2)$$

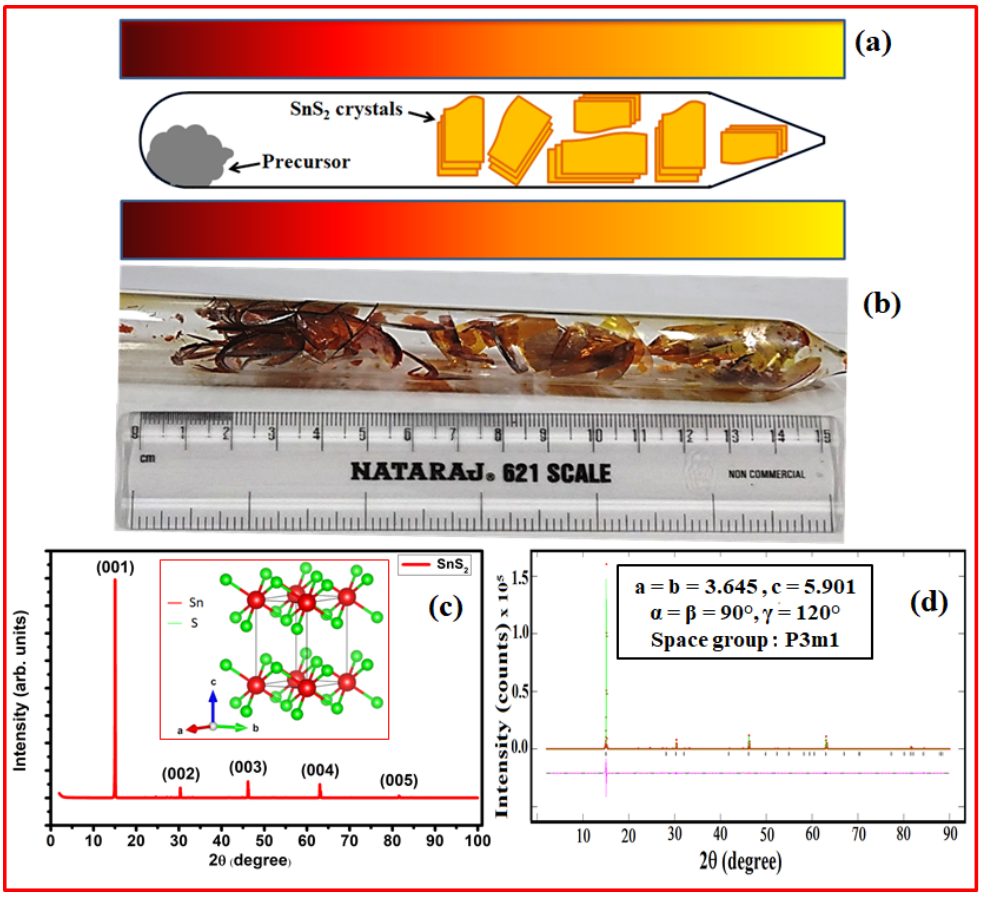

Figure 1. (**a**) Schematic illustration of the CVT process, with the red zone of the furnace indicating higher temperature and the yellow zone indicating lower temperature. (**b**) Optical picture showing high yield of a single crystal of 1 to 2 cm in sealed ampule; (**c**) XRD pattern of a typical SnS_2 single crystal. Inset of (**c**) is the crystal structure of SnS_2 crystal produced with VESTA software. (**d**) Le Bail fitting of SnS_2 single crystal and resulting lattice parameters along with space group (inset).

Once the SnS_2 crystals were grown using the iodine-transported CVT technique, they were further subjected to various characterizations to access their structural, morphological, and optical properties. X-ray diffraction (XRD) is a powerful technique for characterizing the crystal structure of materials, including SnS_2 single crystals. The XRD pattern of

SnS_2 provides information about the crystal symmetry, lattice parameters, crystal quality, and orientation. XRD was used to analyze the precise crystal structures of SnS_2 crystals (Figure 1c), which had (001) preferred orientation that was well indexed to the hexagonal unit cell (JCPDS No. 23-0677) without the presence of other impurity phases. The XRD pattern has a dominant peak at 2θ~15.06° that corresponds to the (001) orientation. A few more peaks with less intensity can be observed at 30.33°, 46.15°, 63.01°, and 81.54° that correspond to (002), (003), (004), and (005), respectively. The narrow width of the strong peaks indicates that the as-grown SnS_2 crystal has excellent crystallinity. The crystal structure of the SnS_2 crystal created using VESTA software is shown in Figure 1c (inset). Le Bail fitting is a common method used to analyze X-ray diffraction (XRD) patterns and extract crystallographic information. It involves fitting the experimental XRD pattern obtained from a single crystal to a calculated or reference pattern, also known as the matching pattern. The Le Bail fitting technique allows for the refinement of crystal structure parameters, such as lattice parameters, atomic positions, and thermal factors, to achieve the best match between the experimental and calculated patterns. Le Bail also fitted XRD patterns (Figure 1d) to display the acquired single-crystal pattern and matching pattern. According to the fitting patterns, the as-prepared SnS_2 single crystal had a standard hexagonal crystal structure with lattice constants of a = b = 3.64 Å, c = 5.90 Å, $\alpha = \beta = 90°$, and $\gamma = 120°$, which belongs to P-3m1 symmetry (space group 164). SnS_2 single crystals grew preferentially along the c-axis, demonstrating a preference for stacking in the (001) direction.

Performing Raman spectroscopy for SnS_2 single crystals provides valuable information about the vibrational modes and crystal structure of the material. SnS_2 belongs to the family of transition metal dichalcogenides (TMDs) and has a layered structure. The Raman spectrum of SnS_2 typically exhibits several prominent peaks corresponding to different vibrational modes. Figure 2a demonstrates the Raman spectrum of the SnS_2 single-crystal taken in backscattering geometry, with the inset showing a magnified spectrum in the range of 185 to 245 cm^{-1}. A sharp and intense peak can be seen about 312 cm^{-1}, with a weaker peak around 212 cm^{-1}. The A_{1g} and E_g phonon modes of SnS_2 are responsible for these peaks, respectively. A_{1g} is known as a singly degenerate active mode where two sulfur (S) atoms move out of phase in respect of one another, although the tin (Sn) atom is stationary. Here, "A" represents a nondegenerate mode and subscript "g" denotes the parity under the inversion of the centrosymmetric space group. The peak E_g at 212 cm^{-1} arises due to in-plane vibration, which has very weak intensity owing to the presence of fewer scattering centers, and, hence, the Rayleigh scattering radiation is feeble [57–59]. Also, the sharp A_{1g} band also reveals the formation of a high-quality SnS_2 single crystal. The Raman spectrum confirms the growth of high-quality SnS_2 with the 2H stacking of the SnS_2 crystal produced via the VESTA software. The schematic vibrational in-plane (E_g) and out-of-plane (A_{1g}) modes of SnS_2 are shown in Figure 2b. Sn and S atoms are depicted by the red and green spheres, respectively. The b and c direction are parallel and perpendicular to the substrate.

Transmission electron microscopy (TEM) and scanning electron microscopy (SEM) are powerful imaging techniques used to study the microstructure and morphology of materials at different scales. Figure 3a is a TEM image of a typical SnS_2 crystal, exhibiting the flaky nature of the crystal. The SAED pattern of the SnS_2 crystal is shown in Figure 3b, demonstrating the hexagonal symmetry of the crystal. Further, the SAED pattern was indexed with the help of Image J software; the first hexagonal ring corresponds to the (001) plane. The result is in good agreement with the demonstrated XRD pattern. Scanning electron microscopy (SEM) was also used to examine the morphology of the as-grown SnS_2 single crystal. The top and cross-sectional-view SEM micrographs of the SnS_2 crystal are shown in Figure 3c,d. The top morphology was uniform and homogeneous with few cracks and holes, as seen in Figure 3c. The SnS_2 films were stacked over each other and formed bulk geometry, as shown in Figure 3d. The SEM micrographs show the formation of bulk SnS_2 crystal geometries stacked regularly, as well as a fairly uniform surface morphology. Total reflection X-ray fluorescence spectroscopy (TXRF) is an analytical technique used to determine the elemental composition and concentration of trace elements in thin films,

surfaces, and liquid samples. It is particularly useful for analyzing samples with low concentrations of elements in the range of parts per billion (ppb) to parts per trillion (ppt). The elemental composition of sulfur (S) at 2.0 to 2.5 keV and tin (Sn) at 3.0 to 3.8 keV can be seen in the TXRF spectrum of the as-synthesized SnS_2 crystal (Figure 3e). The SnS_2 stoichiometry (S/Sn) was found to be ~2.67, which suggests the presence of an excess of sulfur compared to the stoichiometric composition of SnS_2. This might be due to the presence of unreacted or impure sulfur left during the synthesis process.

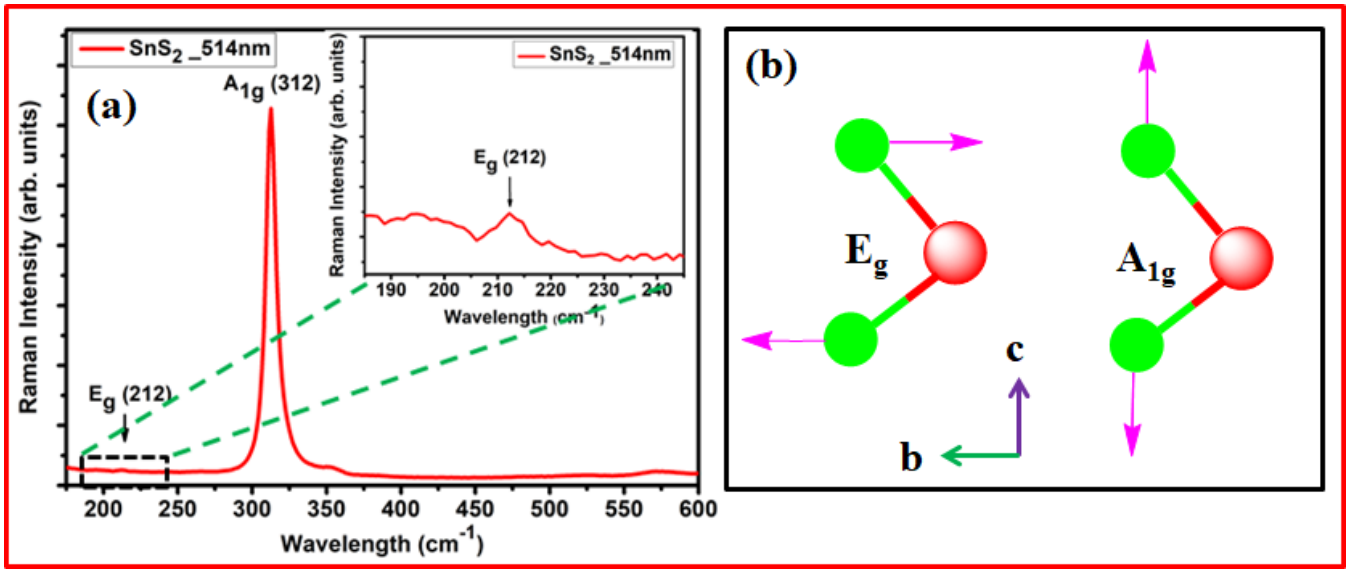

Figure 2. (**a**) Raman spectrum of SnS_2 single crystal with inset showing enlarged spectrum in the region of 185 to 245 cm^{-1}; (**b**) schematic of vibrational in-plane (E_g) and out-of-plane (A_{1g}) modes of SnS_2.

X-ray photoelectron spectroscopy (XPS) is a surface-sensitive analytical technique used to determine the elemental composition, chemical state, and electronic structure of materials. It provides information about the surface chemistry of a sample by measuring the energy distribution of photoelectrons emitted when the sample is irradiated with X-rays. The composition of the as-grown SnS_2 single crystal was characterized using XPS. A representative high-resolution spectrum of the as-produced SnS_2 crystal with binding energies spanning from 0 to 1200 eV is shown in Figure 4a. A variety of peaks in the broad spectrum, including S 2s, double S 2p, doublet Sn 3p, doublet Sn 3d, and Sn 4d, were obtained, demonstrating the presence of Sn and S elements in the SnS_2 crystal. The peaks associated with C and O may have resulted from environmental contamination. There were no other peaks in the spectra that corresponded to other elemental impurities. The high-resolution XPS scans of the Sn 3d and S 2p peaks, respectively, are shown in Figure 4b,c. Two peaks with binding energies of 486.25 eV and 494.65 eV, which correspond to the Sn $3d_{5/2}$ and Sn $3d_{3/2}$ energy levels of Sn atoms in the Sn^{4+} valence state, respectively, were found during a core-level scan of the Sn 3d doublet. Sn $3d_{5/2}$ and Sn $3d_{3/2}$ levels have a maximal splitting energy of about 8.4 eV. The binding energies and spin energy separations of Sn 3d doublets were comparable to those reported [60]. The XPS spectrum of sulfur in the SnS_2 single crystal provides valuable information about the electronic structure and chemical environment of sulfur atoms in the material. The S 2p XPS spectrum typically exhibits two major peaks: the S $2p_{3/2}$ and S $2p_{1/2}$ peaks, which correspond to the binding energy of the sulfur 2p electrons. The S $2p_{3/2}$ peak represents the binding energy of the sulfur $2p_{3/2}$ electrons. This peak arises from the transitions of electrons from the $2p_{3/2}$ level to higher energy states. The S $2p_{3/2}$ peak appears at a lower binding energy than the S $2p_{1/2}$ peak due to spin–orbit splitting. The S $2p_{1/2}$ peak appears at a higher binding energy and is usually less intense compared to the S $2p_{3/2}$ peak. It arises from the transitions of electrons from the $2p_{1/2}$ level to higher energy states. The presence of a single-phase SnS_2 in the as-grown

SnS_2 crystal was confirmed by the presence of two peaks (Figure 4c) with binding energies of 162.50 eV and 161.35 eV, respectively, that correspond to the S $2p_{1/2}$ and S $2p_{3/2}$ energy levels of S atoms in the Sn^{2-} valence state. The interpretation of these peaks suggests that the S atoms in SnS_2 are bonded to Sn atoms in the Sn^{4+} oxidation state, forming $S^{2-} - Sn^{4+}$ bonds. This is consistent with the energies of the $S^{2-} - Sn^{4+}$ bond [60,61].

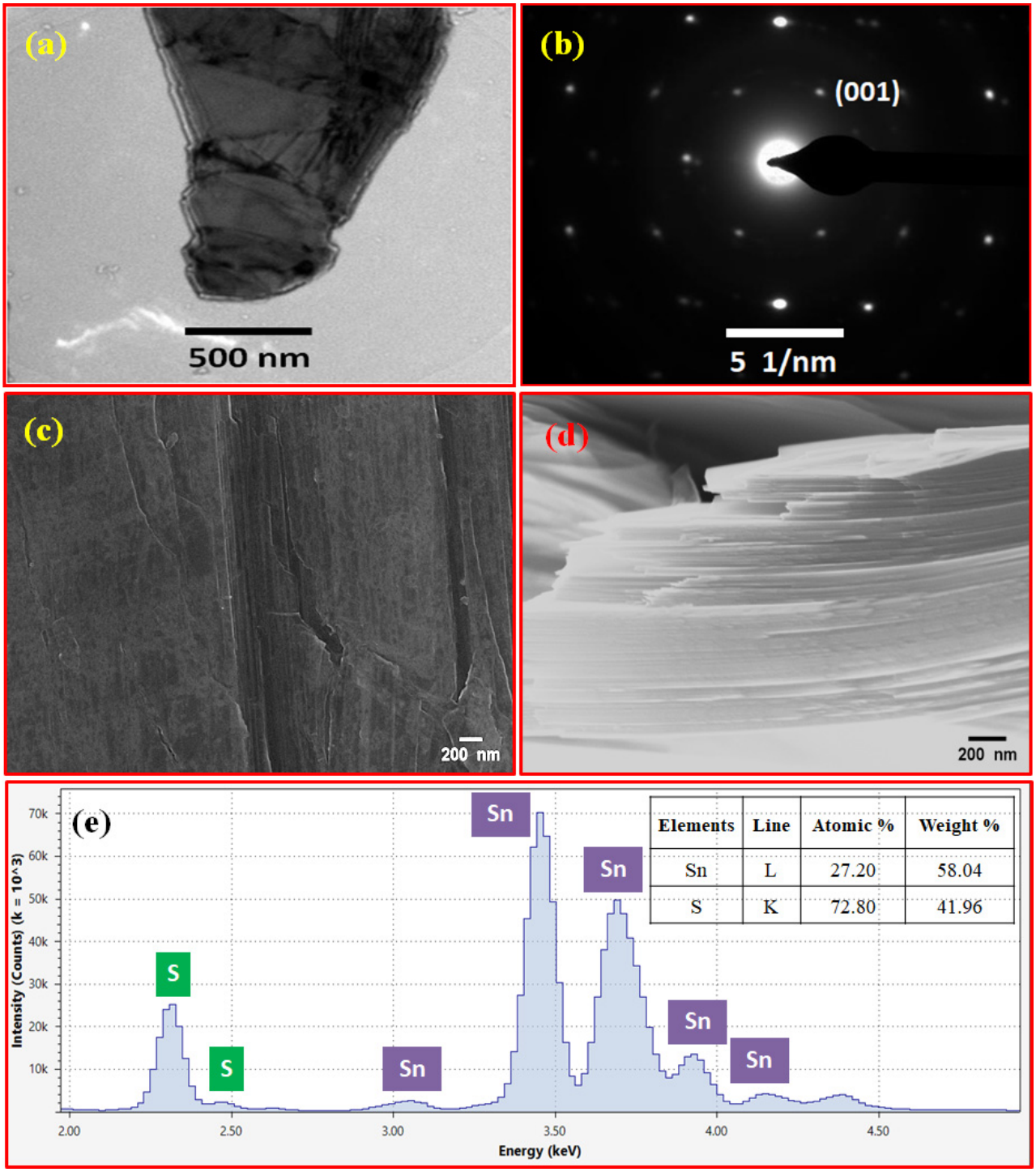

Figure 3. (**a**) A typical TEM micrograph and (**b**) SAED pattern of SnS_2 crystal. SEM micrographs of a single crystal of SnS_2; (**c**) top view, (**d**) cross-sectional view, and (**e**) TXRF spectrum and corresponding elemental composition of Sn and S in Figure 1c.

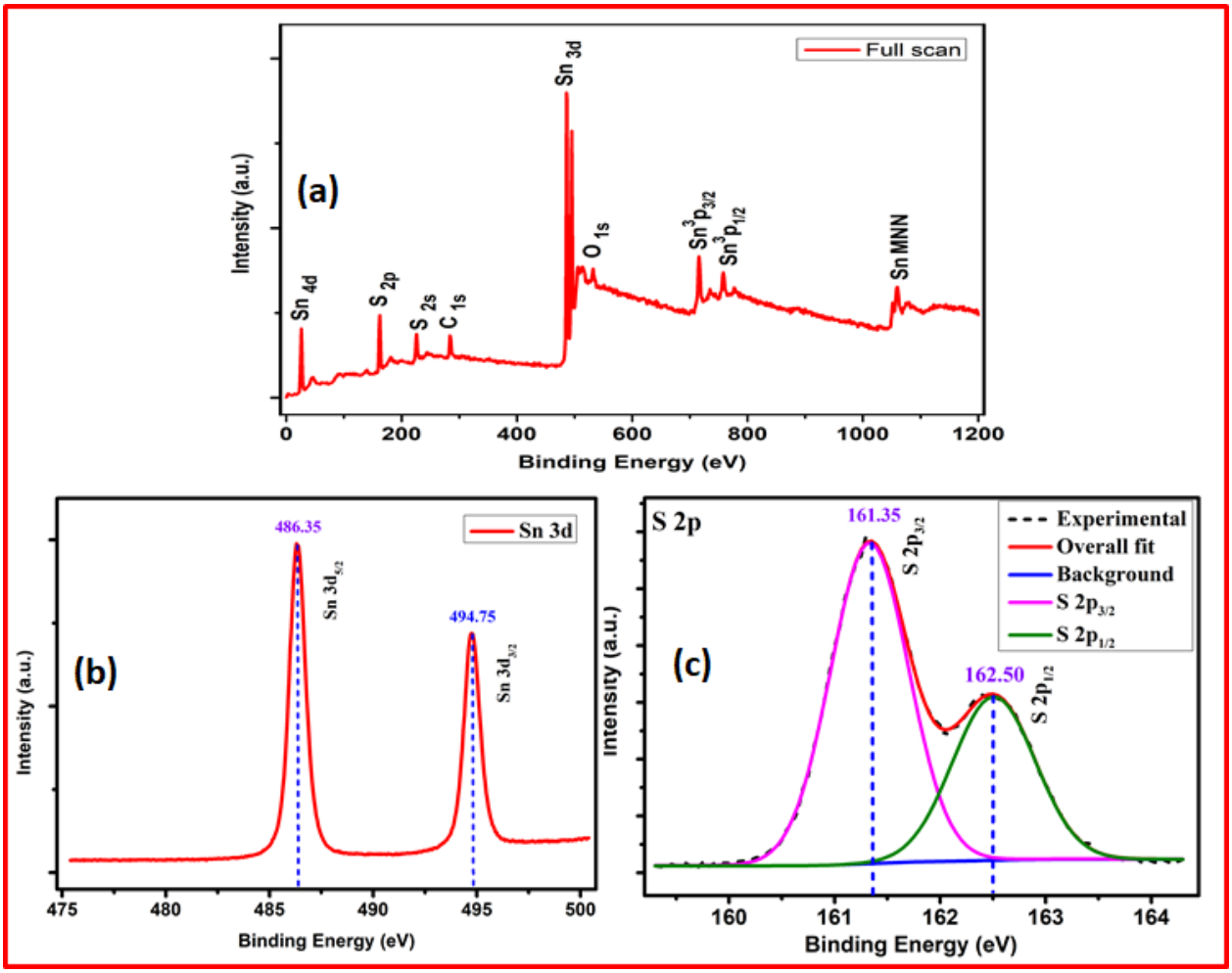

Figure 4. (**a**) Full-scan XPS spectrum and high-resolution scan of core-level (**b**) Sn 3d and (**c**) S 2p SnS_2 crystal.

UV–Vis (ultraviolet–visible) and PL (photoluminescence) spectroscopy are two commonly used techniques for characterizing the optical properties of materials, including semiconductors, quantum dots, organic compounds, and nanoparticles. UV–Vis spectroscopy measures the absorption or transmission of light in the ultraviolet and visible regions of the electromagnetic spectrum. It provides information about the electronic transitions and energy levels of materials. Figure 5a shows the UV–Vis spectrum of a solid SnS_2 crystal recorded in absorbance mode over a broad wavelength range of 200–800 nm. The converted Kubelka–Munk function $((\alpha h\upsilon)^{1/2})$ vs. photon energy ($h\upsilon$) plot for SnS_2 is shown in Figure 5b. The absorption coefficient α and photon energy ($h\upsilon$) is related by the equation:

$$(\alpha h\nu)^n = A(h\upsilon - E_g) \quad (3)$$

The absorption coefficient and optical bandgap are represented by α and E_g, respectively. A is proportionality constant and n = 1/2 for indirect and n = 2 for direct bandgap transitions. The intercept of the linear part on the photon energy axis provides the optical bandgap and was found to be 2.15 eV in this case, which is similar to the bandgap reported earlier [45,62].

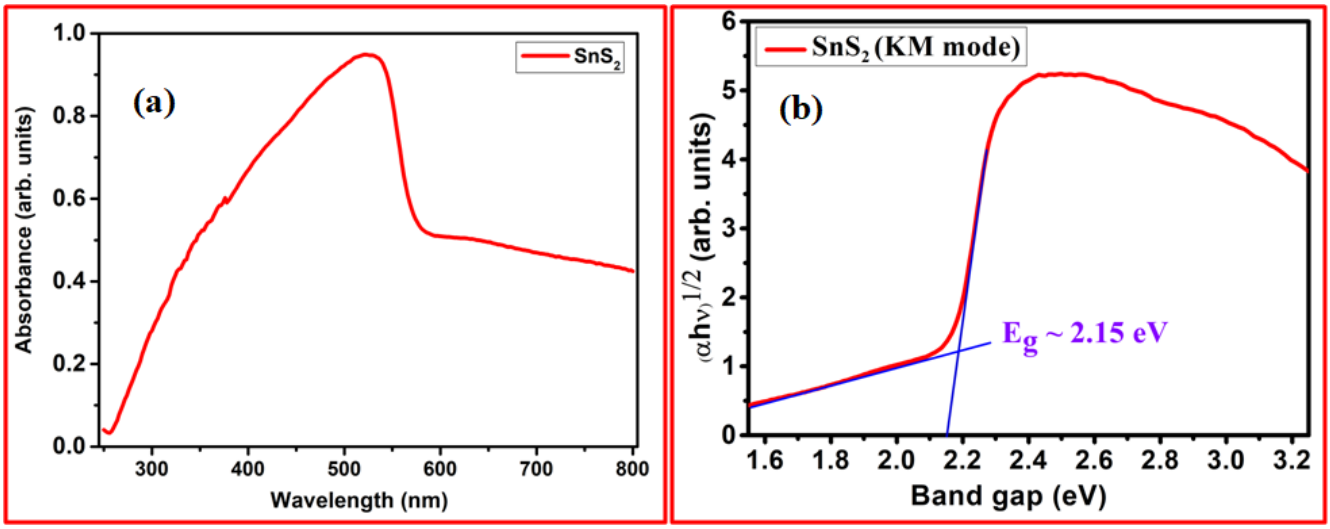

Figure 5. (**a**) UV–Vis spectrum and (**b**) corresponding K-M mode spectrum of SnS_2 single crystal.

Photoluminescence (PL) is a spectroscopic technique used to analyze the spectrum emitted by the radiative recombination of photoinduced minority carriers. It provides insights into the photophysical processes, energy levels, and defects within the material. The PL emission spectrum of a SnS_2 crystal (Figure 6a) was measured at room temperature in the wavelength range of 470 to 688 nm with an excitation wavelength of 355 nm. The spectrum exhibits a strong and broad peak at around 572 nm, which correlates to red emission. This peak (~2.16 eV) arises due to the radiative recombination of bound excitons (electron–hole pairs) and this recombination of excitons occurs via the absorption of electron present at higher excited energy levels. The measured spectrum matches the UV–Vis spectra shown in Figure 5. The proposed energy band structure of the SnS_2 crystal, derived from the UV–Vis and PL spectrum data, is shown in Figure 6b. The SnS_2 crystal absorbed energy at 3.34 eV (355 nm), excited electrons to an exciting level below conduction, then relaxed to a lower energy level, and ultimately emitted from a height of 2.15 eV (576 nm), returning to the ground state.

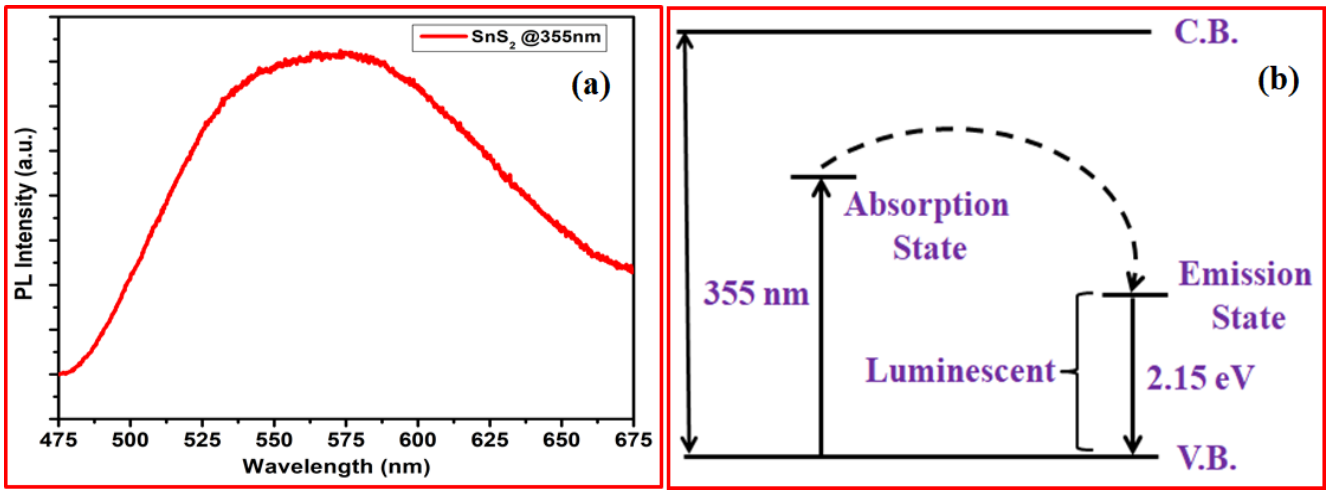

Figure 6. (**a**) PL spectrum and (**b**) proposed energy transfer process in SnS_2 single crystal.

In a nutshell, the acquired results reignite our interest in not only producing large-scale SnS_2 single crystals, but also in further exploring the mechanical exfoliation of these crystals to convert them into high-quality 2D SnS_2 nanosheets, which is our next-level aim for future research.

4. Conclusions

In conclusion, large-scale and high-quality SnS_2 single crystals with large lateral sizes (up to 2 cm) were effectively grown using the iodine-transported CVT approach, and their structural, microstructural, morphological, elemental, and spectroscopic investigations were carried out. The formation of a highly crystalline standard hexagonal crystal structure, with favored preferential orientation growth along the c-axis (001) and lattice constants a = b = 3.64, c = 5.90, $\alpha = \beta = 90^{\circ}$, and $\gamma = 120^{\circ}$, that conforms to P-3m1 symmetry was characterized with X-ray diffraction (XRD) and fitted with the Le Bail tool (space group 164). The Raman spectrum also validated the 2H stacking growth of high-quality SnS_2 crystals. The crystal's flaky nature and hexagonal structure were highlighted via TEM and SAED analysis. The bulk geometry of the SnS_2 crystals stacked periodically, as well as an almost uniform surface morphology, was seen in the SEM micrographs. The ratio of the Sn and S, L, and K lines identified with TXRF was also used to calculate the elemental compositions, which were found to be nearly consistent with the SnS_2 stoichiometry. The XPS spectra revealed the presence of Sn and S in the crystal along with a pure SnS_2 phase. UV–visible absorption was used to obtain the optical characteristics, which were validated with PL spectroscopy, which yielded an optical bandgap of 2.15 eV. Based on the chemical reaction involved, a SnS_2 crystal grows in two stages: the transportation of the precursor with the help of iodine, followed by crystal formation at a lower temperature. As a result, this research contributes to a deeper knowledge of the growth of high-quality and large-scale SnS_2 single crystals, as well as their optical properties. This will be tremendously helpful in the preparation of high-quality, tunable-thickness, and large-scale SnS_2 nanosheets, which will aid in the design and development of a variety of advanced optoelectronic and photonic devices.

Author Contributions: Conceptualization, P.T. and B.K.G.; methodology, P.T., A.K. and B.K.G.; Validation, K.S.; investigation, P.T. and A.K.; data curation, P.T., A.K. and P.K.B.; writing—original draft preparation, P.T. and B.K.G.; writing—review & editing, A.K., P.K.B. and K.S.; visualization, K.S.; supervision, B.K.G.; funding acquisition, B.K.G. All authors have read and agreed to the published version of the manuscript.

Funding: This research was funded by the DST-SERB (National Postdoctoral Fellowship Scheme (File No. PDF/2021/001872)) and CSIR (File No. CSIR-SRA 13(9248-A)/2023-PooL).

Data Availability Statement: The data presented in this study are available on reasonable request from the corresponding author.

Acknowledgments: P.T.; one of the authors, would like to thank DST-SERB for the National Postdoctoral Fellowship (File No. PDF/2021/001872). P.K.B. acknowledges the SRA fellowship provided by CSIR (File No. CSIR-SRA 13(9248-A)/2023-PooL). We thank Christian Martella, CNR-IMM for expert assistance with UV-Vis and Raman Spectroscopy. We thank to Meenakshi Pokhriyal, IIT Delhi for her help in Le Bail fitting.

Conflicts of Interest: The authors declare no conflict of interest.

References

1. Abderrahmane, A.; Ko, P.J.; Thu, T.V.; Ishizawa, S.; Takamura, T.; Sandhu, A. High photosensitivity few-layered MoSe2 back-gated field-effect phototransistors. *Nanotechnology* **2014**, *25*, 365202. [CrossRef] [PubMed]
2. Chuang, H.J.; Chamlagain, B.; Koehler, M.; Perera, M.M.; Yan, J.; Mandrus, D.; Tománek, D.; Zhou, Z. Low-resistance 2D/2D ohmic contacts: A universal approach to high-performance WSe2, MoS2, and MoSe2 transistors. *Nano Lett.* **2016**, *16*, 1896–1902. [CrossRef] [PubMed]
3. Di Bartolomeo, A.; Pelella, A.; Urban, F.; Grillo, A.; Iemmo, L.; Passacantando, M.; Liu, X.; Giubileo, F. Field Emission in Ultrathin $PdSe_2$ Back-Gated Transistors. *Adv. Electron. Mater.* **2020**, *6*, 2000094. [CrossRef]
4. Di Bartolomeo, A.; Grillo, A.; Urban, F.; Iemmo, L.; Giubileo, F.; Luongo, G.; Amato, G.; Croin, L.; Sun, L.; Liang, S.-J.; et al. Asymmetric Schottky Contacts in Bilayer MoS_2 Field Effect Transistors. *Adv. Funct. Mater.* **2018**, *28*, 1800657. [CrossRef]
5. Yu, S.H.; Lee, Y.B.; Jang, S.K.; Kang, J.; Jeon, J.; Lee, C.G.; Lee, J.Y.; Kim, H.; Hwang, E.; Lee, S.; et al. Dye-Sensitized MoS2 Photodetector with Enhanced Spectral Photoresponse. *ACS Nano* **2014**, *8*, 8285–8291. [CrossRef]

6. Godde, T.; Schmidt, D.; Schmutzler, J.; Aßmann, M.; Debus, J.; Withers, F.; Alexeev, E.M.; Del Pozo-Zamudio, O.; Skrypka, O.V.; Novoselov, K.S.; et al. Exciton and trion dynamics in atomically thinMoSe2andWSe2: Effect of localization. *Phys. Rev. B* **2016**, *94*, 165301. [CrossRef]
7. Guo, J.; Yang, B.; Zheng, Z.; Jiang, J. Observation of abnormal mobility enhancement in multilayer MoS2 transistor by synergy of ultraviolet illumination and ozone plasma treatment. *Phys. E Low-Dimens. Syst. Nanostructures* **2017**, *87*, 150–154. [CrossRef]
8. Huang, Y.; Deng, H.-X.; Xu, K.; Wang, Z.-X.; Wang, Q.-S.; Wang, F.-M.; Zhan, X.-Y.; Li, S.-S.; Luo, J.-W.; He, J. Highly sensitive and fast phototransistor based on large size CVD-grown SnS_2nanosheets. *Nanoscale* **2015**, *7*, 14093–14099. [CrossRef]
9. Pelella, A.; Grillo, A.; Urban, F.; Giubileo, F.; Passacantando, M.; Pollmann, E.; Sleziona, S.; Schleberger, M.; Di Bartolomeo, A. Gate-Controlled Field Emission Current from MoS2 Nanosheets. *Adv. Electron. Mater.* **2021**, *7*, 2000838. [CrossRef]
10. Shimakawa, K. Electrical Transport Properties. *Mater. Energy* **2021**, 177–202. [CrossRef]
11. Urban, F.; Gity, F.; Hurley, P.K.; McEvoy, N.; Di Bartolomeo, A. Isotropic conduction and negative photoconduction in ultrathin PtSe2 films. *Appl. Phys. Lett.* **2020**, *117*, 193102. [CrossRef]
12. Urban, F.; Passacantando, M.; Giubileo, F.; Iemmo, L.; Di Bartolomeo, A. Transport and Field Emission Properties of MoS_2 Bilayers. *Nanomaterials* **2018**, *8*, 151. [CrossRef] [PubMed]
13. Yang, W.; Shang, J.; Wang, J.; Shen, X.; Cao, B.; Peimyoo, N.; Zou, C.; Chen, Y.; Wang, Y.; Cong, C.; et al. Electrically Tunable Valley-Light Emitting Diode (vLED) Based on CVD-Grown Monolayer WS_2. *Nano Lett.* **2016**, *16*, 1560–1567. [CrossRef] [PubMed]
14. Zhou, X.; Zhang, Q.; Gan, L.; Li, H.; Zhai, T. Large-Size Growth of Ultrathin SnS2 Nanosheets and High Performance for Pho-totransistors. *Adv. Funct. Mater.* **2016**, *26*, 4405–4413. [CrossRef]
15. Lee, C.; Yan, H.; Brus, L.E.; Heinz, T.F.; Hone, J.; Ryu, S. Anomalous Lattice Vibrations of Single- and Few-Layer MoS_2. *ACS Nano* **2010**, *4*, 2695–2700. [CrossRef]
16. Mak, K.F.; Lee, C.; Hone, J.; Shan, J.; Heinz, T.F. Atomically thin MoS2: A new direct-gap semiconductor. *Phys. Rev. Lett.* **2010**, *105*, 2–5. [CrossRef]
17. Ramasubramaniam, A. Large excitonic effects in monolayers of molybdenum and tungsten dichalcogenides. *Phys. Rev. B* **2012**, *86*, 115409. [CrossRef]
18. Chernikov, A.; Berkelbach, T.C.; Hill, H.M.; Rigosi, A.; Li, Y.; Aslan, O.B.; Reichman, D.R.; Hybertsen, M.S.; Heinz, T.F. Exciton binding energy and nonhydrogenic Rydberg series in monolayer WS2. *Phys. Rev. Lett.* **2014**, *113*, 1–5. [CrossRef]
19. Radisavljevic, B.; Radenovic, A.; Brivio, J.; Giacometti, V.; Kis, A. Single-layer MoS2 transistors. *Nat. Nanotechnol.* **2011**, *6*, 147–150. [CrossRef]
20. Sanne, A.; Ghosh, R.; Rai, A.; Yogeesh, M.N.; Shin, S.H.; Sharma, A.; Jarvis, K.; Mathew, L.; Rao, R.; Akinwande, D.; et al. Radio Frequency Transistors and Circuits Based on CVD MoS_2. *Nano Lett.* **2015**, *15*, 5039–5045. [CrossRef]
21. Fan, C.; Li, Y.; Lu, F.; Deng, H.-X.; Wei, Z.; Li, J. Wavelength dependent UV-Vis photodetectors from SnS_2 flakes. *RSC Adv.* **2016**, *6*, 422–427. [CrossRef]
22. Furchi, M.M.; Pospischil, A.; Libisch, F.; Burgdörfer, J.; Mueller, T. Photovoltaic Effect in an Electrically Tunable van der Waals Heterojunction. *Nano Lett.* **2014**, *14*, 4785–4791. [CrossRef] [PubMed]
23. Deng, L.; Zhu, Z.; Liu, L.; Liu, H. Synthesis of Ag2O and Ag co-modified flower-like SnS2 composites with enhanced photocatalytic activity under solar light irradiation. *Solid State Sci.* **2017**, *63*, 76–83. [CrossRef]
24. Hu, Y.; Chen, T.; Wang, X.; Ma, L.; Chen, R.; Zhu, H.; Yuan, X.; Yan, C.; Zhu, G.; Lv, H.; et al. Controlled growth and photo-conductive properties of hexagonal SnS2 nanoflakes with mesa-shaped atomic steps. *Nano Res.* **2017**, *10*, 1434–1447. [CrossRef]
25. Jia, X.; Tang, C.; Pan, R.; Long, Y.-Z.; Gu, C.; Li, J. Thickness-Dependently Enhanced Photodetection Performance of Vertically Grown SnS_2 Nanoflakes with Large Size and High Production. *ACS Appl. Mater. Interfaces* **2018**, *10*, 18073–18081. [CrossRef]
26. Yang, Y.B.; Dash, J.K.; Xiang, Y.; Wang, Y.; Shi, J.; Dinolfo, P.H.; Lu, T.-M.; Wang, G.-C. Tuning the Phase and Optical Properties of Ultrathin SnSx Films. *J. Phys. Chem. C* **2016**, *120*, 13199–13214. [CrossRef]
27. Gong, Y.; Yuan, H.; Wu, C.-L.; Tang, P.; Yang, S.-Z.; Yang, A.; Li, G.; Liu, B.; van de Groep, J.; Brongersma, M.L.; et al. Spatially controlled doping of two-dimensional SnS2 through intercalation for electronics. *Nat. Nanotechnol.* **2018**, *13*, 294–299. [CrossRef]
28. Manzeli, S.; Ovchinnikov, D.; Pasquier, D.; Yazyev, O.V.; Kis, A. 2D transition metal dichalcogenides. *Nat. Rev. Mater.* **2017**, *2*, 17033. [CrossRef]
29. Zhou, X.; Hu, X.; Zhou, S.; Song, H.; Zhang, Q.; Pi, L.; Li, L.; Li, H.; Lü, J.; Zhai, T. Tunneling Diode Based on WSe2 /SnS2 Het-erostructure Incorporating High Detectivity and Responsivity. *Adv. Mater.* **2018**, *30*, 1703286. [CrossRef]
30. Fu, X.; Ilanchezhiyan, P.; Kumar, G.M.; Cho, H.D.; Zhang, L.; Chan, A.S.; Lee, D.J.; Panin, G.N.; Kang, T.W. Tunable UV-visible absorption of SnS_2layered quantum dots produced by liquid phase exfoliation. *Nanoscale* **2017**, *9*, 1820–1826. [CrossRef]
31. Xia, J.; Zhu, D.; Wang, L.; Huang, B.; Huang, X.; Meng, X.-M. Large-Scale Growth of Two-Dimensional SnS_2Crystals Driven by Screw Dislocations and Application to Photodetectors. *Adv. Funct. Mater.* **2015**, *25*, 4255–4261. [CrossRef]
32. Yang, T.; Zheng, B.; Wang, Z.; Xu, T.; Pan, C.; Zou, J.; Zhang, X.; Qi, Z.; Liu, H.; Feng, Y.; et al. Van der Waals epitaxial growth and optoelectronics of large-scale WSe2/SnS2 vertical bilayer p–n junctions. *Nat. Commun.* **2017**, *8*, 1906. [CrossRef] [PubMed]
33. Ying, H.; Li, X.; Wu, Y.; Yao, Y.; Xi, J.; Su, W.; Jin, C.; Xu, M.; He, Z.; Zhang, Q. High-performance ultra-violet phototransistors based on CVT-grown high quality SnS_2flakes. *Nanoscale Adv.* **2019**, *1*, 3973–3979. [CrossRef] [PubMed]

34. Giri, B.; Masroor, M.; Yan, T.; Kushnir, K.; Carl, A.D.; Doiron, C.; Zhang, H.; Zhao, Y.; McClelland, A.; Tompsett, G.A.; et al. Balancing Light Absorption and Charge Transport in Vertical SnS $_2$ Nanoflake Photoanodes with Stepped Layers and Large Intrinsic Mobility. *Adv. Energy Mater.* **2019**, *9*, 1901236. [CrossRef]
35. Zhang, Y.; Zhu, P.; Huang, L.; Xie, J.; Zhang, S.; Cao, G.; Zhao, X. Few-Layered SnS_2on Few-Layered Reduced Graphene Oxide as Na-Ion Battery Anode with Ultralong Cycle Life and Superior Rate Capability. *Adv. Funct. Mater.* **2014**, *25*, 481–489. [CrossRef]
36. Zhang, Z.; Huang, J.; Zhang, M.; Yuan, Q.; Dong, B. Ultrathin hexagonal SnS2 nanosheets coupled with g-C3N4 nanosheets as 2D/2D heterojunction photocatalysts toward high photocatalytic activity. *Appl. Catal. B: Environ.* **2015**, *163*, 298–305. [CrossRef]
37. Wang, B.; Zhong, S.P.; Bin Zhang, Z.; Zheng, Z.Q.; Zhang, Y.P.; Zhang, H. Broadband photodetectors based on 2D group IVA metal chalcogenides semiconductors. *Appl. Mater. Today* **2019**, *15*, 115–138. [CrossRef]
38. Zhu, H.L.; Cheng, J.; Zhang, D.; Liang, C.; Reckmeier, C.J.; Huang, H.; Rogach, A.L.; Choy, W.C.H. Room-Temperature Solu-tion-Processed NiOx:PbI2 Nanocomposite Structures for Realizing High-Performance Perovskite Photodetectors. *ACS Nano* **2016**, *10*, 6808–6815. [CrossRef]
39. Song, H.S.; Li, S.L.; Gao, L.; Xu, Y.; Ueno, K.; Tang, J.; Cheng, Y.B.; Tsukagoshi, K. High-performance top-gated monolayer SnS2 field-effect transistors and their integrated logic circuits. *Nanoscale* **2013**, *5*, 9666–9670. [CrossRef]
40. Su, G.; Hadjiev, V.G.; Loya, P.E.; Zhang, J.; Lei, S.; Maharjan, S.; Dong, P.; Ajayan, P.M.; Lou, J.; Peng, H. Chemical Vapor Deposition of Thin Crystals of Layered Semiconductor SnS2 for Fast Photodetection Application. *Nano Lett.* **2015**, *15*, 506–513. [CrossRef]
41. Wen, S.; Pan, H.; Zheng, Y. Electronic properties of tin dichalcogenide monolayers and effects of hydrogenation and tension. *J. Mater. Chem. C* **2015**, *3*, 3714–3721. [CrossRef]
42. Zschieschang, U.; Holzmann, T.; Kuhn, A.; Aghamohammadi, M.; Lotsch, B.V.; Klauk, H. Threshold-voltage control and enhancement-mode characteristics in multilayer tin disulfide field-effect transistors by gate-oxide passivation with an alkylphosphonic acid self-assembled monolayer. *J. Appl. Phys.* **2015**, *117*, 104509. [CrossRef]
43. Fu, Y.; Gou, G.; Wang, X.; Chen, Y.; Wan, Q.; Sun, J.; Xiao, S.; Huang, H.; Yang, J.; Dai, G. High-performance photodetectors based on CVD-grown high-quality SnS2 nanosheets. *Appl. Phys. A* **2017**, *123*, 1–8. [CrossRef]
44. Wang, S.; Yu, H.; Zhang, H.; Wang, A.; Zhao, M.; Chen, Y.; Mei, L.; Wang, J. Broadband Few-Layer MoS2 Saturable Absorbers. *Adv. Mater.* **2014**, *26*, 3538–3544. [CrossRef]
45. Liu, W.; Liu, M.; Wang, X.; Shen, T.; Chang, G.; Lei, M.; Deng, H.-X.; Wei, Z.; Wei, Z.-Y. Thickness-Dependent Ultrafast Photonics of SnS_2 Nanolayers for Optimizing Fiber Lasers. *ACS Appl. Nano Mater.* **2019**, *2*, 2697–2705. [CrossRef]
46. Vyas, S.M.; Desai, C.F.; Desai, C.F.; Shah, R.C.; Pandya, G.R. Microhardness Creep in Single Crystals of Tin-chalcogenides. *Turk. J. Phys.* **2000**, *24*, 21–27.
47. Kana, A.; Hibbert, T.; Mahon, M.; Molloy, K.; Parkin, I.; Price, L. Organotin unsymmetric dithiocarbamates: Synthesis, formation and characterisation of tin(II) sulfide films by atmospheric pressure chemical vapour deposition. *Polyhedron* **2001**, *20*, 2989–2995. [CrossRef]
48. Nair, P.; Nair, M.; García, V.; Arenas, O.; Peña, A.C.Y.; Ayala, I.; Gomezdaza, O.; Sánchez, A.; Campos, J.; Hu, H.; et al. Semiconductor thin films by chemical bath deposition for solar energy related applications. *Sol. Energy Mater. Sol. Cells* **1998**, *52*, 313–344. [CrossRef]
49. Kim, J.Y.; George, S.M. Tin Monosulfide Thin Films Grown by Atomic Layer Deposition Using Tin 2,4-Pentanedionate and Hydrogen Sulfide. *J. Phys. Chem. C* **2010**, *114*, 17597–17603. [CrossRef]
50. Ghazali, A.; Zainal, Z.; Hussein, M.Z.; Kassim, A. Cathodic electrodeposition of SnS in the presence of EDTA in aqueous media. *Sol. Energy Mater. Sol. Cells* **1998**, *55*, 237–249. [CrossRef]
51. Sugiyama, M.; Miyauchi, K.; Minemura, T.; Ohtsuka, K.; Noguchi, K.; Nakanishi, H. Preparation of SnS Films by Sulfurization of Sn Sheet. *Jpn. J. Appl. Phys.* **2008**, *47*, 4494–4495. [CrossRef]
52. Xu, Z.; Chen, Y. Fabrication of SnS thin films by a novel multilayer-based solid-state reaction method. *Semicond. Sci. Technol.* **2012**, *27*, 35007. [CrossRef]
53. Ghosh, B.; Das, M.; Banerjee, P.; Das, S. Fabrication and optical properties of SnS thin films by SILAR method. *Appl. Surf. Sci.* **2008**, *254*, 6436–6440. [CrossRef]
54. Schäfer, H.; Jacob, H.; Etzel, K.; Chemische Transportreaktionen. II. Die Verwendung der Zerfallsgleichgewichte der Eisen(II)- und Nickel(II)-halogenide zum Metalltransport im Temperaturgefälle, Z. *Anorg. Allg. Chem.* **1956**, *286*, 42–55. [CrossRef]
55. Nitsche, R.; Bölsterli, H.; Lichtensteiger, M. Crystal growth by chemical transport reactions—I. *J. Phys. Chem. Solids* **1961**, *21*, 199–205. [CrossRef]
56. Colombara, D.; Delsante, S.; Borzone, G.; Mitchels, J.; Molloy, K.; Thomas, L.; Mendis, B.; Cummings, C.; Marken, F.; Peter, L. Crystal growth of Cu2ZnSnS4 solar cell absorber by chemical vapor transport with I2. *J. Cryst. Growth* **2012**, *364*, 101–110. [CrossRef]
57. Wang, Y.; Huang, L.; Wei, Z. Photoresponsive field-effect transistors based on multilayer SnS_2 nanosheets. *J. Semicond.* **2017**, *38*, 034001. [CrossRef]
58. Voznyi, A.; Kosyak, V.; Opanasyuk, A.; Tirkusova, N.; Grase, L.; Medvids, A.; Mezinskis, G. Structural and electrical properties of SnS2 thin films. *Mater. Chem. Phys.* **2016**, *173*, 52–61. [CrossRef]
59. Sriv, T.; Kim, K.; Cheong, H. Low-Frequency Raman Spectroscopy of Few-Layer 2H-SnS2. *Sci. Rep.* **2018**, *8*, 10194. [CrossRef]

60. Gedi, S.; Alhammadi, S.; Noh, J.; Reddy, V.R.M.; Park, H.; Rabie, A.M.; Shim, J.-J.; Kang, D.; Kim, W.K. SnS_2 Nanoparticles and Thin Film for Application as an Adsorbent and Photovoltaic Buffer. *Nanomaterials* **2022**, *12*, 282. [CrossRef]
61. Crist, B.V. *Handbook of Monochromatic XPS Spectra*; Wiley: Chichester, UK; New York, NY, USA, 2000.
62. Burton, L.A.; Colombara, D.; Abellon, R.D.; Grozema, F.C.; Peter, L.M.; Savenije, T.J.; Dennler, G.; Walsh, A. Synthesis, Characterization, and Electronic Structure of Single-Crystal SnS, Sn_2S_3, and SnS_2. *Chem. Mater.* **2013**, *25*, 4908–4916. [CrossRef]